Research Square

Preprints are preliminary reports that have not undergone peer review.
They should not be considered conclusive, used to inform clinical practice,
or referenced by the media as validated information.

Solidification cracking mechanism in 15Cr-15Ni Ti-stabilised fully austenitic stainless steel welds for nuclear core components

R Ravikumar
Indira Gandhi Centre for Atomic Research
M Divya
Indira Gandhi Centre for Atomic Research
S Sampreeth
Indian Institute of Technology
Chitta Ranjan Das
chitta@igcar.gov.in

Indira Gandhi Centre for Atomic Research https://orcid.org/0000-0002-7210-498X

Research Article

Keywords: Alloy D9I, Solidification cracking susceptibility, Segregation, Equilibrium phase diagram, Scheil's solidification model

Posted Date: September 7th, 2026

DOI: https://doi.org/10.21203/rs.3.rs-10469890/v1

License: This work is licensed under a Creative Commons Attribution 4.0 International License.
Read Full License

Solidification cracking mechanism in 15Cr-15Ni Ti-stabilised fully austenitic stainless steel welds for nuclear core components

R.Ravikumar[1, 2], M. Divya[1], S. Sampreeth[3], C.R.Das*[1,2]
[1]Indira Gandhi Centre for Atomic Research, Kalpakkam, India, 603102
[2]Homi Bhabha National Institute, Kalpakkam, India, 603102
[3]Indian Institute of Technology, Kharagpur, India
*chitta@igcar.gov.in

Abstract

The influence of phosphorus (P), silicon (Si), and titanium (Ti) contents on the solidification cracking susceptibility of fully austenitic 15Cr–15Ni–Ti stabilised stainless steel was investigated using the Varestraint test. The results demonstrated that the susceptibility to solidification cracking increased significantly with increasing phosphorus and silicon contents. In addition, steels with a higher Ti/(C + 0.856N) ratio exhibited a lower threshold strain for crack initiation than those with a lower Ti/(C + 0.856N) ratio and lower impurity contents, indicating an increased tendency for solidification cracking. The combined effect of elevated impurity levels and a higher Ti/(C + 0.856N) ratio altered the composition and distribution of the terminal eutectic phases formed during weld solidification, thereby influencing the cracking resistance of the alloy. Based on the experimental observations, the mechanism of solidification cracking in 15Cr–15Ni–Ti-stabilised stainless steel is discussed with respect to alloy composition and the evolution of eutectic phases during solidification.

Keywords: Alloy D9I, Solidification cracking susceptibility, Segregation, Equilibrium phase diagram, Scheil's solidification model.

1. Introduction

Alloy D9, a modified 316 austenitic stainless steel strengthened by 20% cold work, is extensively used as a core structural material in sodium-cooled fast reactors owing to its excellent high-temperature strength and irradiation resistance [1,2]. However, the achievable fuel burn-up in fast reactors is largely limited by the void-swelling resistance of core structural materials during prolonged neutron irradiation [3]. In the absence of oxide-dispersion-strengthened (ODS) cladding tubes on an industrial scale, a modified version of Alloy D9, designated as D9I (Indian Fast Reactor Advanced Cladding, Version-1 or IFAC-1), has been developed to achieve higher fuel burn-up and improved irradiation performance in Fast Breeder Reactors (FBRs) [4].

To enhance swelling resistance, the phosphorus, silicon, and boron contents in D9I have been deliberately increased relative to those in Alloy D9 [2,3]. The elevated phosphorus and silicon contents promote the formation of stable phosphate and silicide precipitates during service, which act as effective vacancy sink sites and thereby reduce void swelling [3]. Although these alloying modifications improve irradiation performance, they are expected to adversely affect weldability. The detrimental influence of impurity elements such as sulfur and phosphorus on the solidification cracking susceptibility of austenitic stainless steels is well established [5–7]. Similarly, increased silicon content has been reported to reduce the

resistance of the alloy to solidification cracking [8]. Boron, owing to its extremely low solubility in iron and strong segregation tendency during solidification, can further increase cracking susceptibility by promoting the formation and persistence of low-melting inter-dendritic liquid films [9].

The low Cr_{eq}/Ni_{eq} ratio (~1) of D9I promotes primary austenitic (A-mode) solidification. Combined with the elevated concentrations of phosphorus, silicon, and boron, this solidification mode renders the alloy particularly susceptible to solidification cracking during welding [10]. Yamashita et al. have shown that 310 SS, which solidifies in primary austenite mode, reveals the highest cracking susceptibility as compared to 304, 410, 430, and 329J3L stainless steels due to higher segregation of impurity elements [11]. Solidification cracking in austenitic stainless steels and nickel-based alloys is influenced by several factors, including solidification mode, alloy chemistry, segregation behaviour of minor alloying elements, strain imposed during solidification, and welding parameters [5–10]. Segregation of alloy/impurity elements to inter-dendritic regions leads to the formation of low-melting eutectics, which broadens the solidification temperature range and prolongs the existence of liquid films during the terminal stages of solidification, thereby increasing cracking susceptibility.

Apart from the influence of minor alloying elements, the Ti/(C+0.857N) ratio has also been reported to significantly affect hot cracking behaviour in Alloy D9. Srinivasan et al. [12] observed increased hot cracking susceptibility in Alloy D9 with a Ti/(C+0.857N) ratio of 3. A higher Ti/(C+0.857N) ratio promotes the formation of TiC, $TiC_{0.3}N_{0.7}$, and carbosulfide precipitates such as Ti_2CS and $Ti_4C_2S_2$. During welding, these precipitates form low-melting eutectic constituents with the surrounding austenitic matrix, thereby increasing the susceptibility to hot cracking [13].

To minimise micro-fissuring during fabrication, Alloy D9 cladding tubes are typically welded to end plugs manufactured from AISI 316L(N) stainless steel, and the weld metal composition is carefully controlled to ensure the formation of a small amount of ferrite during weld solidification [14]. Owing to significantly higher levels of phosphorus, silicon, and boron in D9I, the weldability of this steel is expected to be inferior compared to that of the currently employed D9 alloy. Therefore, an assessment of the solidification cracking susceptibility of D9I is essential prior to its deployment in reactor components.

Accordingly, the present study aims to evaluate the solidification cracking susceptibility of two D9I stainless steel heats possessing Ti/(C+0.857N) ratios of 3.68 and 4.53 using the Varestraint test. The mechanisms governing crack formation are further investigated through detailed microstructural characterisation and thermodynamic analysis, with particular emphasis on the role of solute segregation and Ti/(C+0.857N) ratio in influencing weldability.

2. Experimental Methods

The base material used in this study was received in the form of plates of 12 mm thickness. This steel was melted by Vacuum Induction Melting (VIM) and hot rolled. Chemical compositions of the two heats of Alloy D9I and D9 are given in Table 1. Alloy D9 composition, taken from reference [15], is included for the sake of comparison as it is a predecessor to Alloy D9I. Calphad-based phase transformation simulations of this alloy were carried out using Thermo-Calc™ software version 13 equipped with the TCFe13 database.

Towards understanding the solidification cracking of the present alloy, a systematic study has been taken up using the Transverse Varestraint (Transvarestraint) test.

Table.1 Chemical compositions of Alloy D9I and Alloy D9 in wt.%

Heat No.	Cr	Mn	Mo	Ni	P	Si	Ti	C	N	B	S	Fe
G3088T (HT1)	14.35	2.36	2.40	15.38	0.03	0.74	0.25	0.05	0.01	0.0050	0.005	Bal.
G3055T (HT2)	14.25	1.60	2.37	15.52	0.02	1.00	0.21	0.05	0.008	0.0059	0.006	Bal.
D9	15.1	1.5	2.2	15.04	0.01	0.5	0.21	0.052	0.06	-	0.002	Bal

Varestraint test specimens of dimensions 127 × 25 × 3 mm were fabricated from the as-received alloy plate and used in this study is shown schematically in Fig.1. During Transvarestraint test, an autogenous gas tungsten arc (GTA) weld bead is laid along the transverse direction of the specimen, held firmly on an anvil. Strain is applied pneumatically by bending the specimen as soon as the weld puddle reaches the middle of the specimen. The bending block fixed to the pneumatic ram bends the specimen rapidly. The strain application occurs within 15 milliseconds, such that the weld metal is in the mushy zone. The radius of curvature of the bending block attached to the ram controls the amount of strain imparted to the specimen. The relationship between the radius of curvature and strain experienced by the specimen is given by the expression

$e = t/(2r+t)$

where,

e is the strain experienced by the outer fibre of the specimen.

t is the thickness of the specimen.

r is the radius of the die block.

Four strain levels, namely, 0.25%, 0.5%, 1%, 2%, and 4% were applied just by changing the bending blocks with different radii of curvature. At each strain level, 3 specimens were tested. This procedure was repeated for the specimens made out of different heats. This procedure is similar to that adopted in reference [4]. After the Transvarestraint tests, all tested specimens were pickled to remove the oxide layer from the weld bead using a pickling solution (1% HF + 20% HNO_3 + 79% methanol). Crack lengths on the surface of the tested specimens were measured at 1.6X magnification using a stereo microscope. Specimens for microstructural analysis were extracted from the hot crack-tested specimens and prepared by grinding and polishing using standard grids of emery papers followed by diamond slurry up to 1 μm surface finish. These specimens were then electrochemically etched using 10% oxalic acid at 3V DC for 10 seconds. These specimens were then characterised using a light optical microscope and a Scanning Electron Microscope / Energy dispersive spectroscopy (SEM/EDS) for microstructural analysis.

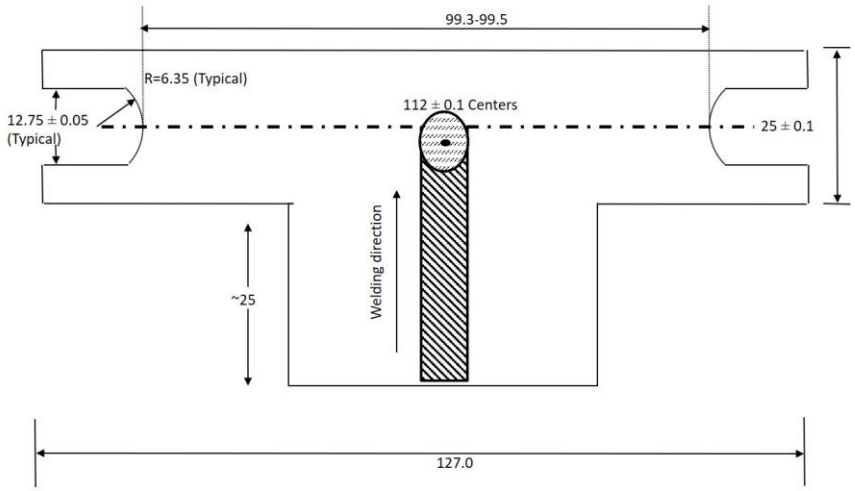


Fig.1 Drawing of Transvarestraint test specimen showing the direction of GTA welding during the execution of the Varestraint test.

3. Results

3.1 Base metal microstructure

Fig. 2 shows the photomicrographs of HT1 and HT2 of Alloy D9I SS, which reveal austenite grains containing primary MX-type precipitates in the austenite matrix. The average grain size for both heats is ~ 80-100 µm. The MX-type precipitates are indicated by arrow marks in the microstructures in Fig.2. These primary precipitates are identified as Ti(C,N) using EDS in SEM [16].

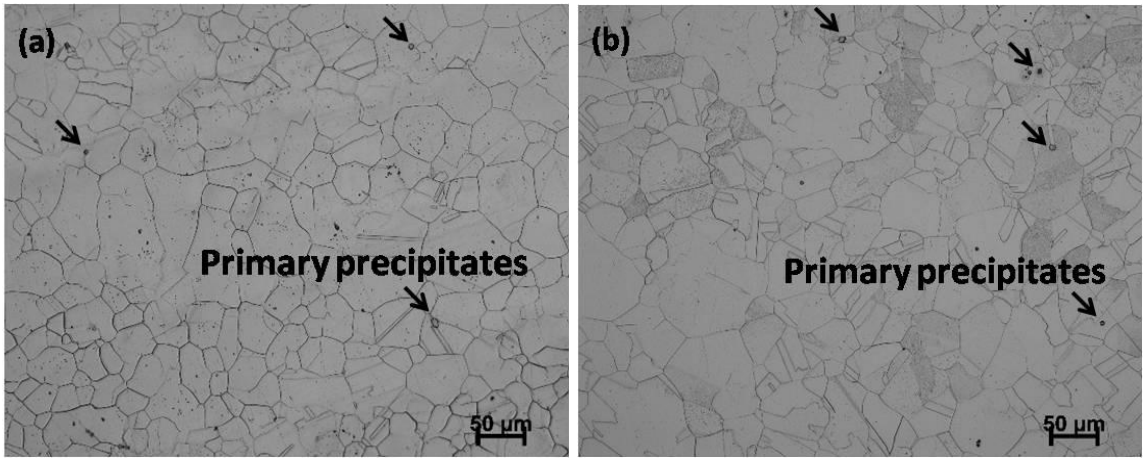


Fig. 2 Microstructure of Alloy D9I (a) HT1 (b) HT2 obtained using a light optical microscope; the arrows indicate primary precipitates in the matrix.

3.2 Equilibrium and non-equilibrium phase transformations in Alloy D9I

Thermo-Calc^{TM} calculations were carried out to understand the equilibrium phase transformations in Alloy D9I HT1 and HT2, and the results are shown in Fig.3. From these figures, it is evident that the heats of Alloy D9I solidify in primary austenitic mode. The predicted equilibrium phase transformation sequence as a function of decreasing temperature from the liquid is listed below.

Ti(C,N) is the first phase to form from the liquid at 1450 °C.

$L \leftrightarrow L + \gamma$ (1425 °C)

$L + \gamma \leftrightarrow L + Ti_4C_2S_2 + \gamma$ (1400 °C)

$L + Ti_4C_2S_2 + \gamma \leftrightarrow \gamma + M_3B_2$ (1390 °C)

$\gamma + M_3B_2 \leftrightarrow \gamma + M_3B_2 +$laves (825 °C)

$\gamma +$ laves$\leftrightarrow \gamma +$ laves $+ M_{23}C_6 + \alpha + \alpha`$ (575 °C)

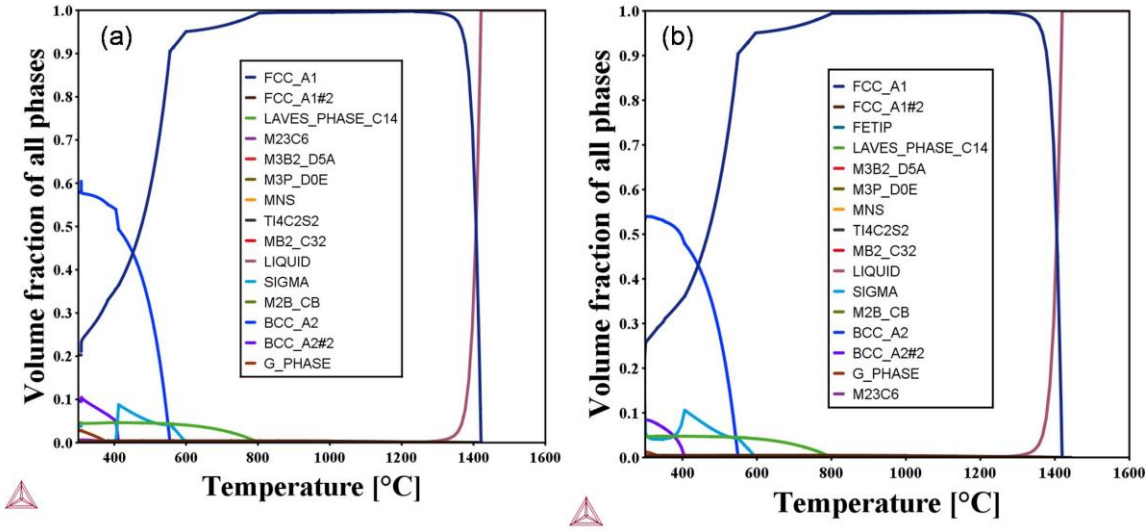


Fig.3 Equilibrium phase diagram of (a) HT1 and (b) HT2 calculated using Thermo-Calc^{TM} software version 13 equipped with TCFE 13 database.

It is to be noted that both heats (HT1 and HT2) of Alloy D9I follow the same solidification sequence except for the formation of FeTiP precipitates in HT2 and minor variations in the fractions of the Ti(C,N) and $Ti_4C_2S_2$. According to the equilibrium phase diagrams, the solidification range for HT1 and HT2 is 175 ºC and 185 ºC, respectively. It is worth noting that the calculations were performed, including all probable phases present in the alloy system. Accordingly, the phase diagram also shows the presence of sigma phase, G phase and Laves phases, although these phases form only after prolonged ageing, in addition to commonly seen phases in the steel [17].

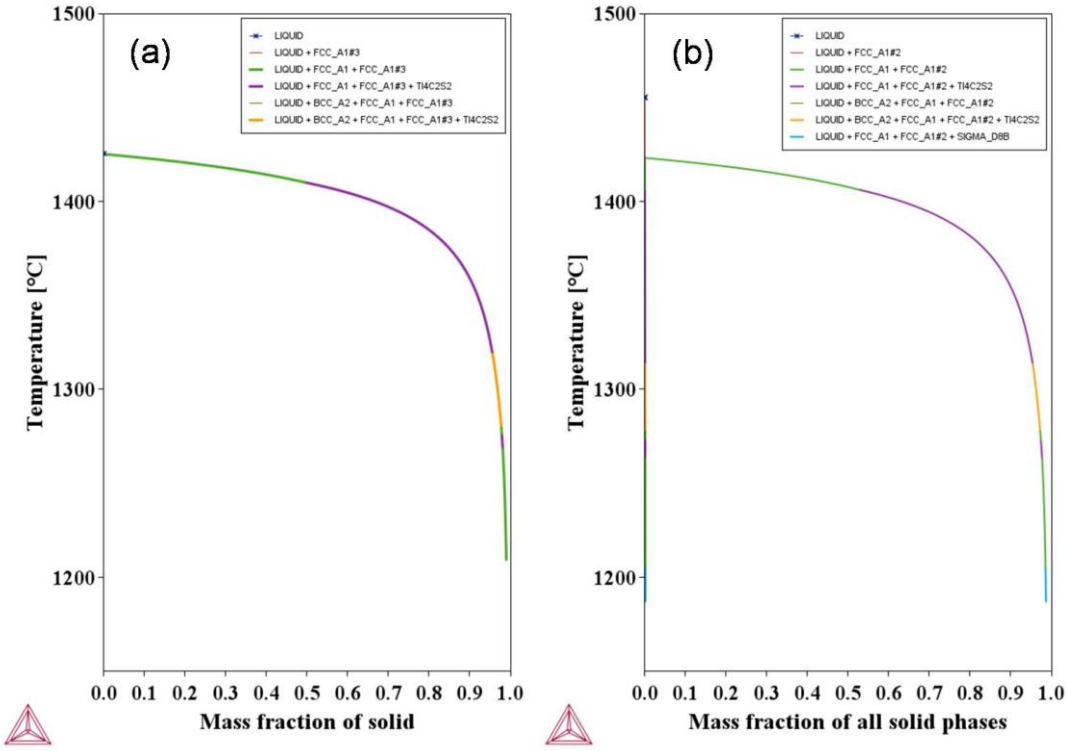


Fig. 4 Scheil's solidification simulation of Alloy D9I (a) HT1 and (b) HT2 performed using Thermo-Calc^{TM} software.

It is to be noted that non-equilibrium cooling conditions prevail during solidification, which leads to segregation of alloying elements (C and N are taken as fast-diffusing elements) at the solid-liquid interface, resulting in the formation of non-equilibrium phases in the fusion zone. These phases deviate from those of the equilibrium predictions. The phases present in the fusion zone are dictated by the instantaneous composition of the liquid at the solid/liquid interface and the prevailing kinetic conditions. Hence, the solidification process of the alloy under non-equilibrium conditions is simulated using Scheil's solidification module in Thermo-Calc^{TM} software. Fig. 4 shows the mass fraction of solid formed from the liquid as a function of decreasing temperature. From this figure, it is observed that the solidification starts at 1425 °C, where the mass fraction of solid is zero. This temperature is taken as the liquidus. At 1410 °C, about 50 percent of the phase fraction corresponds to austenite, and the remaining liquid is richer in Ti. At this temperature, the Ti-rich $Ti_4C_2S_2$ precipitation occurs. At about 1325 °C, a 0.05 fraction of delta ferrite forms in the last to solidify liquid. Subsequently, the ferrite phase transforms to austenite at 1210 °C just before the completion of the solidification process. This temperature (1210 °C) marks the solidus of the alloy during non-equilibrium cooling for HT1, whereas the same temperature is 1190 °C for HT2, as shown in Fig. 4(b). In HT2, the solidification process starts earlier (1450 °C) than that of HT1 and proceeds further by precipitation of sigma phase until the fraction of liquid tends to zero. It is noteworthy that the phenomenon of ferrite formation in the last to solidify liquid exists even in the case of HT2 at 1320 °C. The solidification range of the Alloy D9I taken in this study, under non-equilibrium conditions, is ~ 210 - 230 °C, which is 175 - 185 °C for equilibrium conditions. Comparison of the equilibrium and non-equilibrium solidification

sequences reveals that there is a significant variation in the solidification range due to segregation of alloying elements during solidification.

3.3 Solidification cracking susceptibility

Fig.5 shows variations of Maximum Crack Length (MCL) vs. % augmented strain and Total Crack Length (TCL) vs. % augmented strain measured from the Transvarestraint tested specimens of HT1 and HT2 heats, respectively. From these figures, it is evident that the MCL and TCL of both heats increase monotonically with increasing augmented strain. It is also evident from the figure that the hot cracking propensity of HT2 is high compared to that of HT1 in all augmented strains. It is also clear from the figure that the threshold strain for cracking is 0.25 % for both the heats, which indicates higher susceptibility for cracking as compared to Alloy D9 (0.5%), reported in [16]. The MCL at 4 % strain (saturated strain) is ~ 1.7 and 2.8 mm, respectively, for HT1 and HT2 heats. The MCL value for both heats is more than thrice compared to that of Alloy D9 (~0.26 mm) [16]. This suggests that alloy D9I is more susceptible to cracking compared to Alloy D9 even at lower restraints

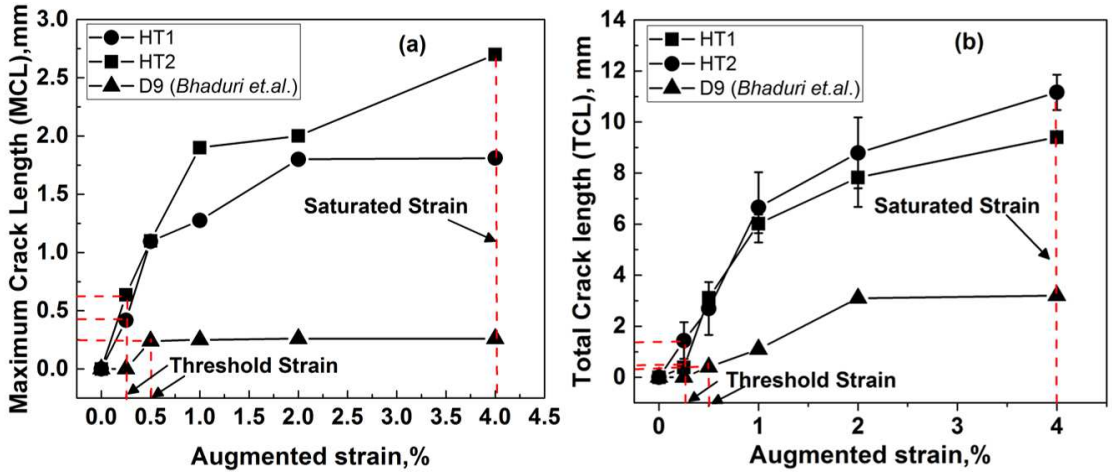


Fig.5 Comparison of solidification cracking susceptibilities of HT1 and HT2 heats using (a) plot of Maximum Crack Length (MCL) vs. % Augmented strain, (b) plot of Total Crack Length (MCL) vs. % augmented strain data obtained from Transvarestraint tests.

Microstructures of Transvarestraint tested specimen are shown in Fig.6. Numerous solidification cracks are evident around the instantaneous solid/liquid interface in both heats of the Alloy D9I. From the high-magnification images in the inset of the figures, it is distinctly discernible that the cracks are inter-dendritic in nature in both heats of the alloy.

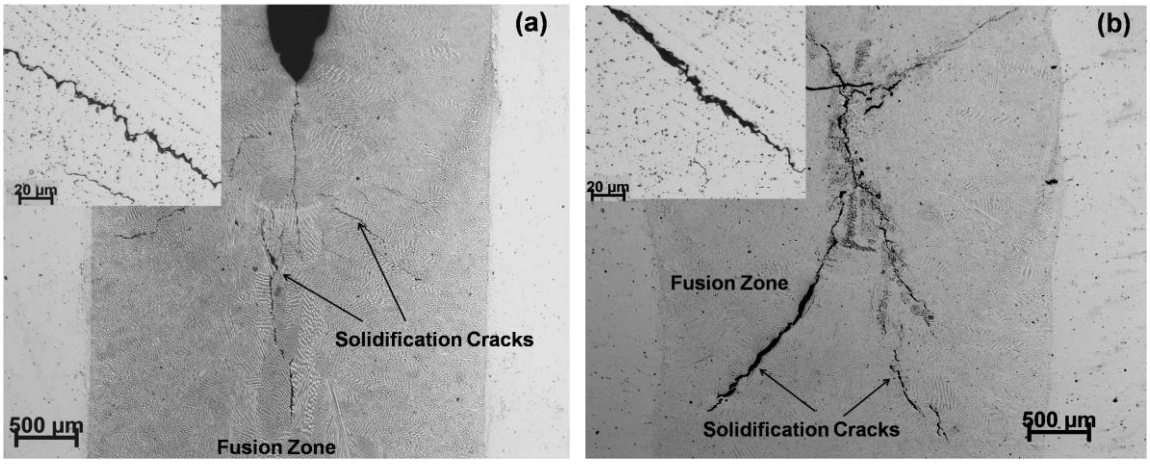
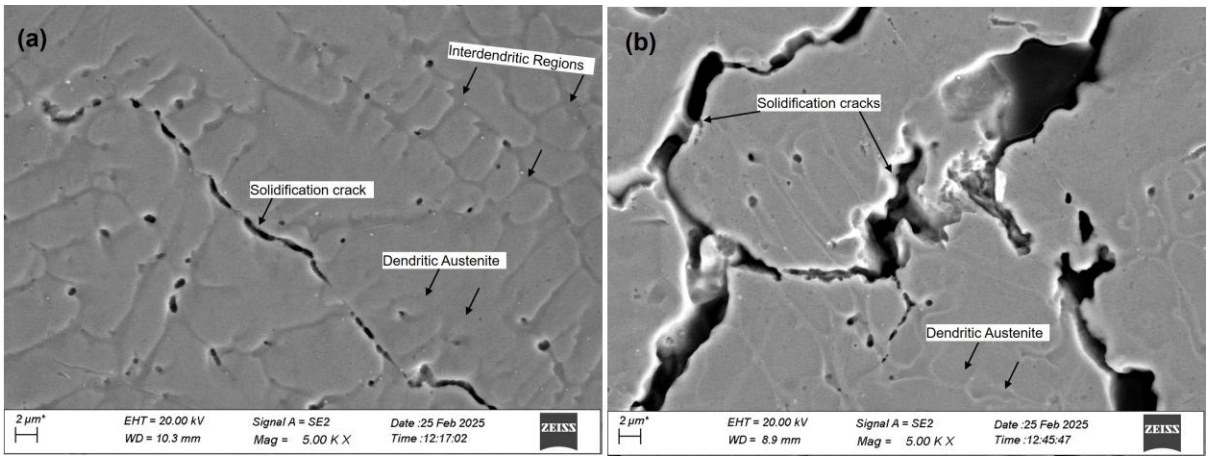


Fig.6 Microstructure of fusion zone of Varestraint tested (a) HT1 and (b) HT2 specimens tested at 0.5% augmented strain. In the inset of the images, high-magnification microstructures are shown.

3.4. Microchemistry of fusion zone

Fig. 7 shows the SE images of the fusion zone and EDS spectra from the region of interest. SE images of the fusion zone show dendritic microstructure in which inter-dendritic cracks are discernible in both heats. EDS point analysis was carried out on dendritic cores and inter-dendritic regions of the fusion zone. It is to be noted that the compositions obtained through EDS analysis are semi quantitative only for major and minor transition metals, for other impurity elements, the values are qualitative and used for comparison purposes, light elements like C, B and N cannot be determined using this technique. The measured compositions of the alloying elements are listed in Table 2.



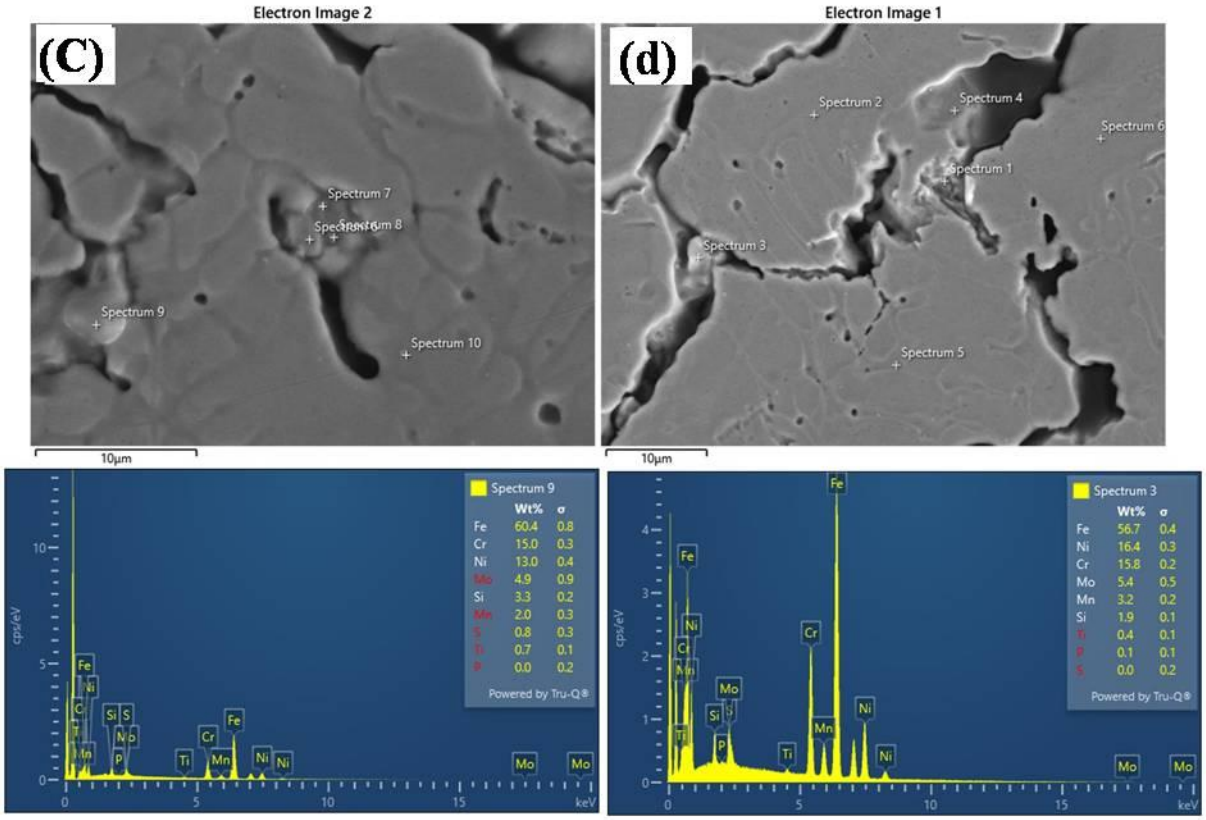


Fig. 7 SE images of fusion zones of Transvarestraint tested (a) HT1 and (b) HT2 heats, EDS spectra from Energy Dispersive Spectra of (c) HT1 and (d) HT2.

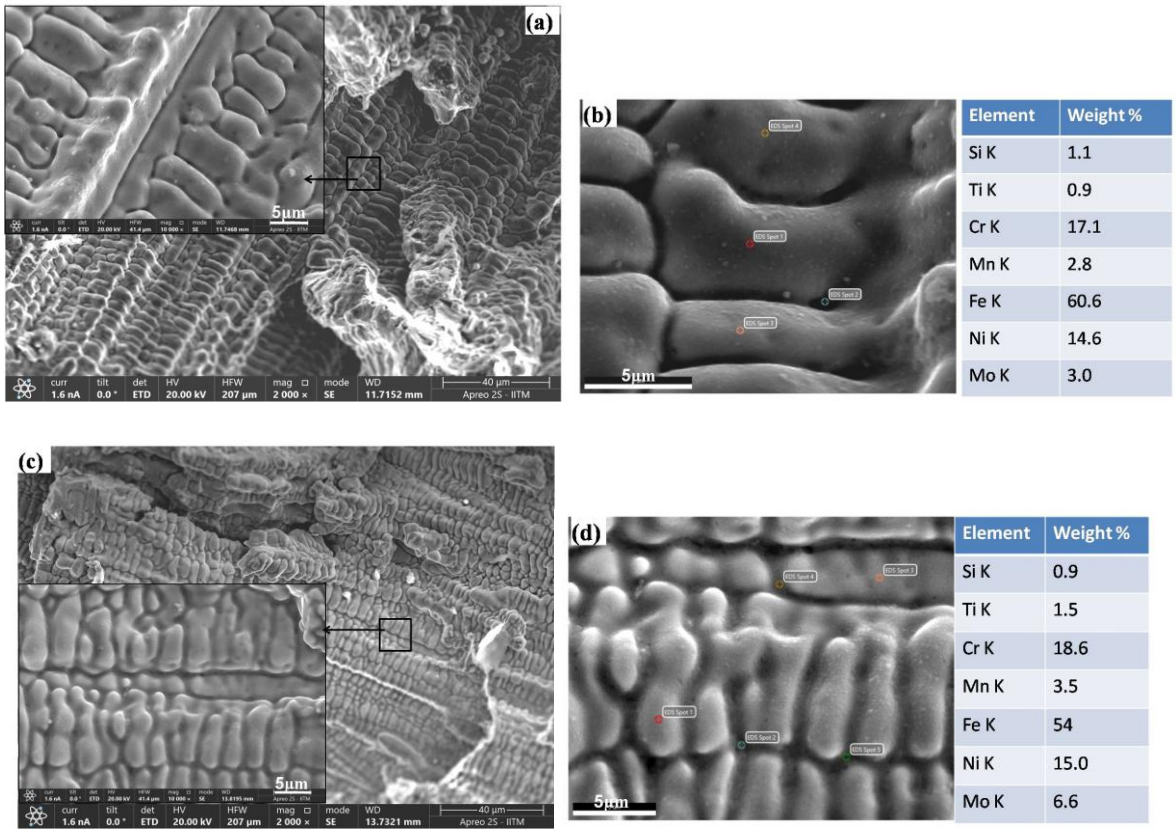
Table 2. Microchemistry of the fusion zone of Alloy D9I - HT1 and HT2 obtained using SEM/EDS spot analysis in Wt.%.

Elements	Alloy D9I HT1			Alloy D9I HT2		
	Average composition at dendrite core (C_d)	Average composition at dendrite boundary (C_i)	Partitioning ratio (C_d/C_i)	Average composition at dendrite core (C_d)	Average composition at dendrite boundary(C_i)	Partitioning Ratio (C_d/C_i)
Fe	64.85±0.84	65.1±12.53	0.99	65.55±0.49	59.88±4.85	1.09
Ni	14.55±0.26	15.7±0.44	0.92	14.6±0.28	14.8±5.31	0.77
Cr	14.52±0.129	15.35±1.18	0.94	14.3±0.07	15.1±1.01	0.94
Mo	2.5±0.25	4.2±0.39	0.59	2.4±0.21	3.58±1.03	0.67
Mn	2.35±0.23	2.7±0.43	0.87	2.2	2.58±0.56	0.85
Si	1.22±0.09	2.15±0.57	0.58	0.7±0.07	1.1±0.44	0.63
Ti	0.17±0.05	0.5±0.10	0.34	0.1±0.07	1.45±3.01	0.06
P	0	0.1*	-	0	0.1*	-
S	0	0	-	0	0.1*	-

* The values shown are indicative only.

From the EDS results given in Table 2, it is evident that there is severe segregation of alloying elements like Mo, Mn, Si, Ti, and P, as well as impurity element S. Among these, the most deleterious elements that expand the freezing temperature range and cause solidification cracking are Mo, Si, Ti, P and S.

3.5Fractography of the solidification cracks



Element	Weight %
Si K	1.1
Ti K	0.9
Cr K	17.1
Mn K	2.8
Fe K	60.6
Ni K	14.6
Mo K	3.0

Element	Weight %
Si K	0.9
Ti K	1.5
Cr K	18.6
Mn K	3.5
Fe K	54
Ni K	15.0
Mo K	6.6

Fig.8 Fractographs of solidification cracks obtained from Alloy D9I after Transvarestraint test at 4% augmented strain (a) HT-1(b) HT-1, SEM/EDS analysis on fracture surface (c) HT-2 (d) HT-2, SEM/EDS taken at the interdendritic sites on fracture surface.

Fig. 8 shows the fractographs of the solidification cracks in the fusion zone of Alloy D9I, HT-1 and HT-2 heats. The fractographs were obtained using SEM by carefully opening the solidification cracks formed at a 4% augmented-strain-tested specimen. The fractographs clearly show the “egg-crate” morphology of solidification cracks in both heats.

The dendritic and interdendritic morphologies observed on the fracture surfaces exhibit clear evidence of liquid wetting, confirming that cracking occurred during the terminal stages of solidification. SEM/EDS analysis performed on the dendritic and interdendritic regions of the fracture surfaces reveals a greater degree of solute segregation in the HT-2 alloy than in the HT-1 alloy. In particular, the interdendritic regions of HT-2 exhibit higher concentrations of Mo, Ti, Mn, and Cr, indicating enhanced microsegregation during solidification.

The relatively higher Mn enrichment in the interdendritic regions of HT-2 indirectly suggests increased sulphur segregation, since Mn preferentially reacts with sulphur to form MnS during the final stages of solidification. Although Mn is an austenite stabiliser, its enrichment in the terminal liquid is primarily governed by solute partitioning and its strong chemical affinity for sulphur. The segregation patterns observed on the fracture surfaces are consistent with those obtained from the metallographic specimens extracted from the Varestraint test samples (Fig. 7). The figure also confirms that the crack propagated preferentially through solute-enriched interdendritic regions containing the last solidifying liquid.

4. Discussions

4.1 Effect of Alloy Composition on Solidification Cracking

The Cr and Ni equivalents of Alloy D9I HT1 and HT2 were calculated using the WRC-1992 constitution diagram. The corresponding Cr_{eq}/Ni_{eq} ratios were 0.97 and 0.95, respectively. According to this constitution diagram, alloys with Cr_{eq}/Ni_{eq} values below 1.25 solidify in the fully austenitic (A-mode) solidification mode. The calculated ratios, therefore, indicate that both heats solidify as primary austenite, which is in agreement with the observed weld microstructures containing only austenite dendrites (Fig. 2).

The calculated compositions were further assessed using the Suutala diagram, which predicts solidification cracking susceptibility of stainless steels as a function of composition and Cr_{eq}/Ni_{eq}. Both HT1 and HT2 heats fall within the high-cracking-susceptibility regime owing to their low Cr_{eq}/Ni_{eq} values. This prediction is in agreement with the experimental Varestraint test results, where cracking was observed even at the minimum applied augmented strain (Fig. 5).

The high cracking susceptibility of both heats of steel is attributed to their fully austenitic solidification mode and the segregation of alloying and impurity elements into the inter-dendritic liquid. Thermodynamic calculations indicate that solidification proceeds through primary austenite formation followed by precipitation of Ti(C,N) and $Ti_4C_2S_2$. HT2, possessing a higher value of Ti/(C+0.856N), exhibits earlier precipitation of Ti(C,N), occurring at approximately 1450 °C compared with 1425 °C in HT1. Consequently, a larger fraction of Ti, C and N is removed from the liquid during the early stages of solidification, leaving behind the liquid enriched with P, S, Si, etc.

The higher Ti content in HT2 modifies the composition of the residual liquid and reduces the fraction of $Ti_4C_2S_2$ formed since available C and N are tied up with Ti during the initial stage of solidification. This could promote the formation of TiS, which freezes at a temperature lower than $Ti_4C_2S_2$. However, Scheil's solidification simulation does not predict the formation of TiS in lieu of $Ti_4C_2S_2$ in HT2. Whereas Ti, Mn and Cr segregation is discernable in HT2 specimen as shown in Fig.9 eventhough the nominal composition of Mn in HT2 is 30 percent lower than that of HT1. This observation confirms the formation of TiS in which Mn and other alloy elements are dissolved instead of the formation of $Ti_4C_2S_2$ in HT2. While the S is scavenged by Ti and Mn, P and Si is left enriched in the remaining liquid which depresses the freezing range. Although the equilibrium and Scheil solidification ranges of HT1 and HT2 differ by only about 20°C, this relatively small difference cannot explain the substantially higher cracking susceptibility of HT2. Instead, the results suggest that the redistribution of alloying and impurity elements during non-equilibrium solidification plays a dominant role in controlling the cracking behaviour. This hypothesis is in agreement with EDS elemental mapping of Transvarestraint-tested specimens (Fig. 9) and SEM/EDS spot analysis carried out on the fracture surfaces (Fig.8), which reveals significant segregation of impurities and alloy elements in the inter-dendritic regions adjacent to cracks in HT2 as compared to HT1. These observations confirm that solidification cracking is strongly influenced by localised enrichment of alloy elements rather than by bulk solidification characteristics alone. Similar analysis on the fracture surface of Cast Pin Tear Test (CPTT) specimens of functionally graded filler material (35/45-Si, 35/45-Al and 35/45) used for the

manufacture of pipe components is also shown by Giacomo et al. [18]. The authors carried out extensive SEM/EDS analysis on the fracture surfaces of CPTT specimens of varying filler composition, showcasing the effect of Nb partitioning to the liquid and cascading effect on Cr- carbide precipitations at various stages of solidification in each filler material, which decides its cracking susceptibility.

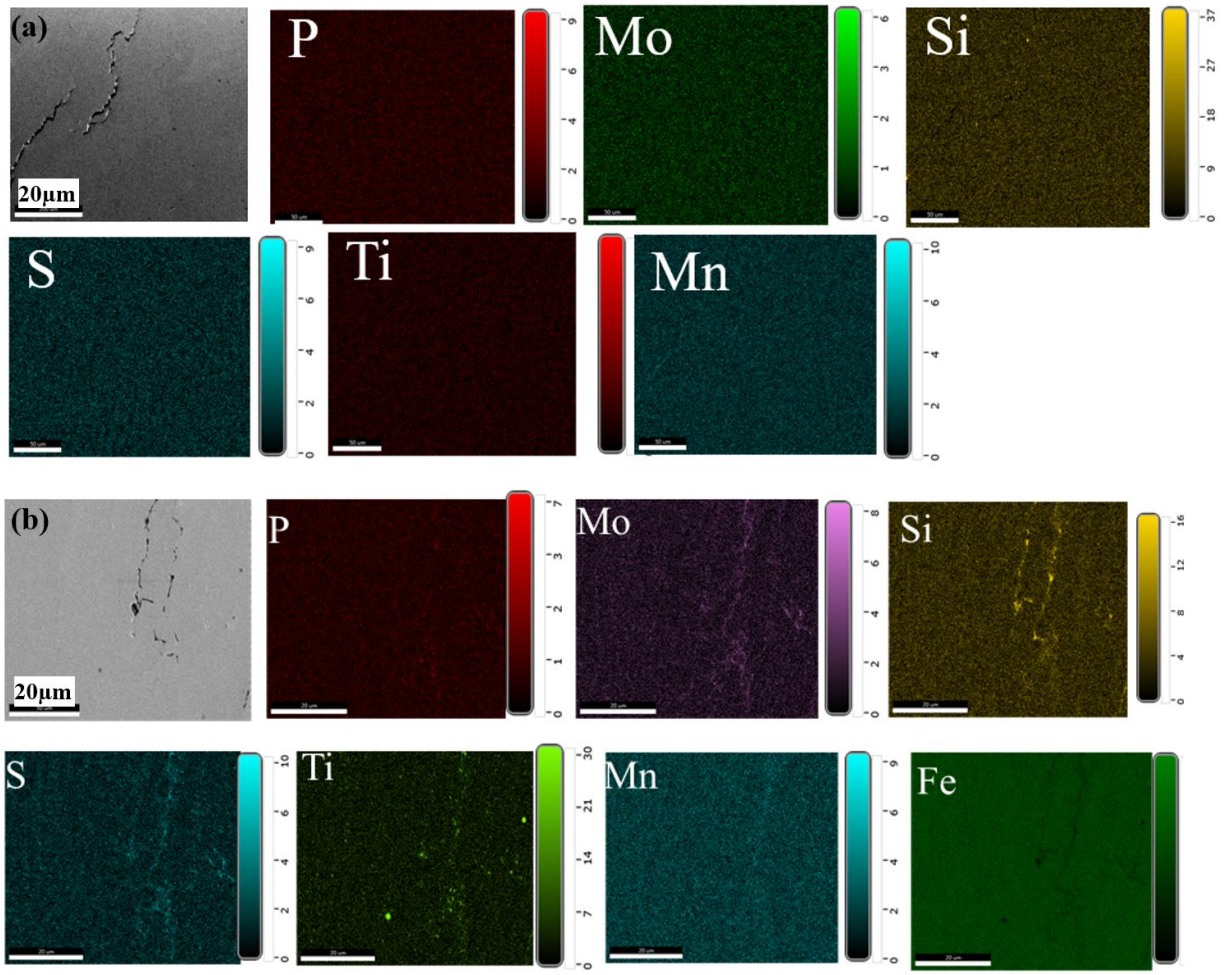


Fig.9 EDS elemental mapping from hot crack tested specimens (a) HT1 (b) HT 2 showing segregation of P, Mo, S, Ti and Mn in the cracked regions.

4.2 Segregation Behaviour of Alloy D9I During Solidification

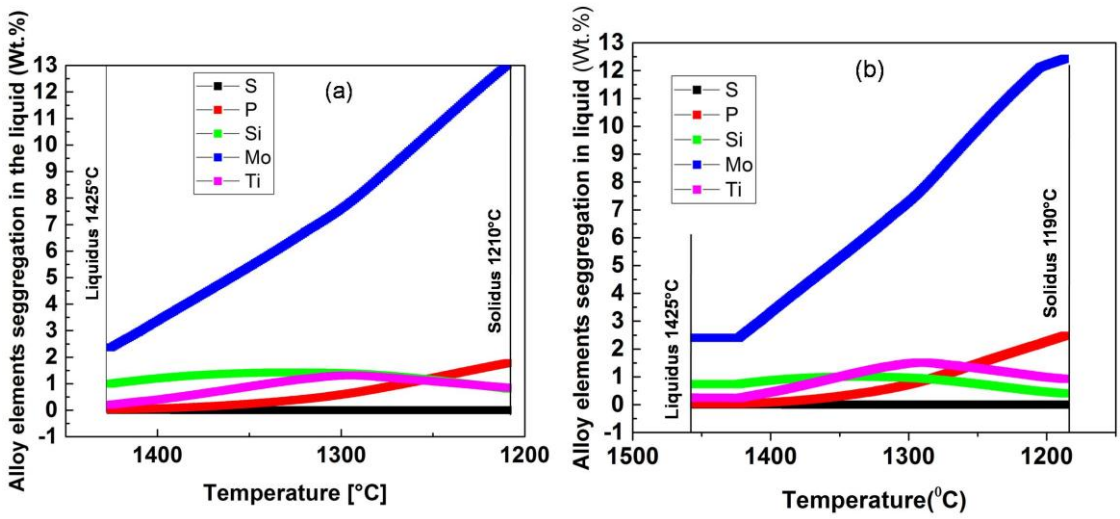


Fig. 10 Segregation of alloying elements in the mushy zone in (a) HT1 and (b) HT2 during the solidification calculated using Scheil's solidification model.

The segregation behaviour of alloying elements during weld solidification was evaluated using Scheil simulations. Figure 10 shows the predicted evolution of Mo, Ti, P, S and Si concentrations in the inter-dendritic liquid as solidification progresses. Strong enrichment of these elements is observed, particularly at solid fractions exceeding 0.9. The calculated partitioning coefficients at approximately 1190 °C in the case of HT1 are about 0.45 for Mo, 0.22 for Ti and 0.01 for P. The calculated partition coefficients at approximately 1190 °C in the case of HT2 are about 0.40 for Mo, 0.17 for Ti and 0.02 for P, indicating increasing segregation tendencies in the order Mo < Ti < P. Folkhard and Matsuda et. al. have reported partitioning coefficients of S, P and Si in austenite as 0.03, 0.13 and 0.52 at high temperature [19,20]. The differences in the values of partitioning coefficient reported in the literature and that obtained in this study can be attributed to variation in temperature at which the values are calculated.

This trend of segregation is in agreement with the calculated values of partitioning ratios obtained from SEM/EDS analysis of dendritic and inter-dendritic regions (Table 2). The partitioning ratio for Mo was approximately 0.59, whereas Ti exhibited a significantly lower value of about 0.06 in HT2. However, the same is about 0.67 and 0.34, respectively, for Mo and Ti in the case of HT1. A significant difference of about one order of magnitude in the calculated and experimentally determined values of partitioning coefficients for Ti in HT2 is observed. This can be attributed to the high reactivity of Ti, which readily forms compounds instead of a solid solution [21]. Quantification of phosphorus and sulphur segregation was not possible because of the limited spatial resolution of EDS; however, their presence was detected at several inter-dendritic locations. Partitioning coefficients of alloy elements at a defined temperature in the austenite phase remain more or less of the same order irrespective of the alloy composition, whereas the enrichment of the alloy elements in the inter-dendritic liquid depends on the alloy composition. That's the reason why the HT2 heat, with a comparatively higher value of Ti/(C+0.856N) than the HT1 heat, shows higher enrichment of Ti in the inter-dendritic liquid than HT1. Similarly, higher enrichment of Mo is observed at

the interdendritic regions on the fracture surface of HT2 than in HT1. Localised enrichment of phosphorus and sulphur was also detected near crack tips in HT2 specimens. Although present in small concentrations, these elements are known to significantly reduce grain-boundary cohesion and promote hot cracking [22].

4.3 Stability of the Interdendritic Liquid

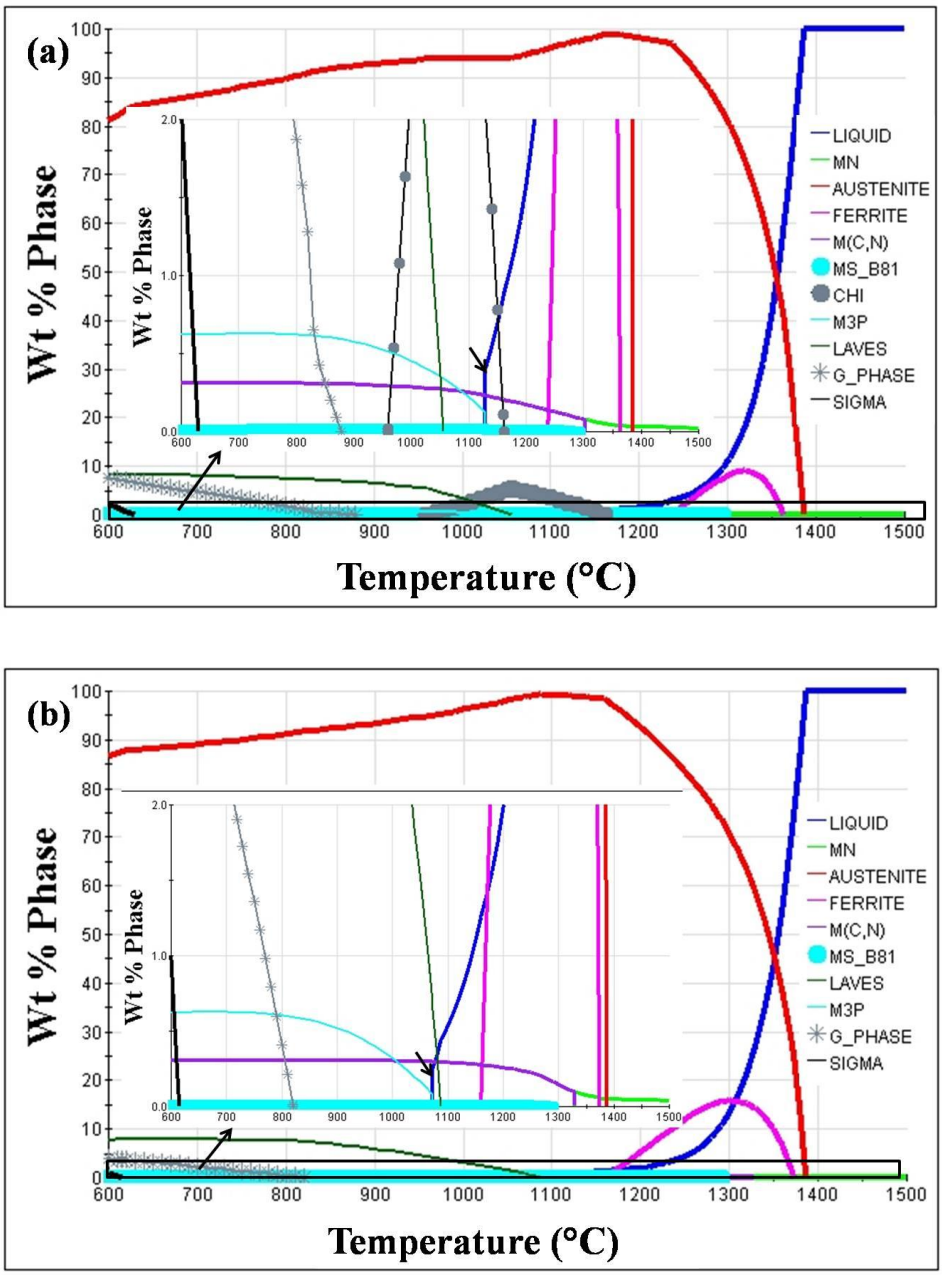


Fig.11 Equilibrium phase diagram calculated using JMatPro^{TM} software for the interdendritic microchemistry of the fusion zone of Alloy D9I obtained from SEM/EDS spot analysis (a) HT1 (b) HT2; the inset figures show a magnified view of the phase diagram demarcated by a rectangle, and the arrows indicate the solidus temperature of the interdendritic compositions.

While equilibrium and Scheil's calculations provide insight into bulk solidification behaviour, solidification cracking is governed primarily by the stability and persistence of the inter-dendritic liquid during the terminal stages of solidification. To evaluate this effect, equilibrium phase-diagram calculations were performed using JMatPro^{TM} software and the measured inter-dendritic compositions.

The calculated phase diagrams, shown in Fig. 11, indicate local solidus temperatures of approximately 1150°C for HT1 and 1075 °C for HT2. These temperatures are substantially lower than those predicted for the bulk compositions, demonstrating the significant influence of solute enrichment on local phase stability.

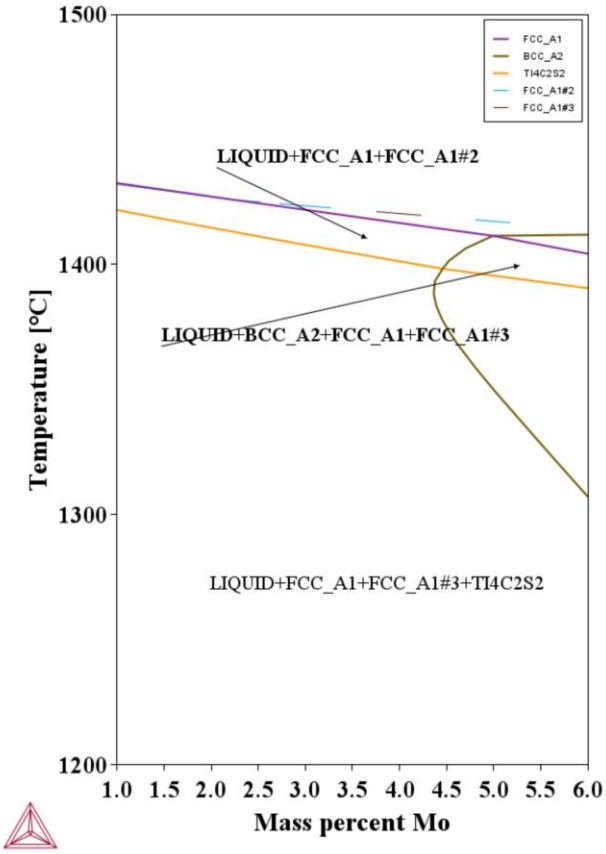


Fig.12 Isopleth (vertical section) of Alloy D9I calculated using Thermo-Calc^{TM} for the HT2 composition

The results show that enrichment of Mo, Si, Ti, P and S stabilises the liquid phase and suppresses the local solidus temperature. This effect is further illustrated by the Mo isopleth calculated using Thermo-Calc^{TM} software for HT2 in Fig.12, which shows progressive solidus depression with increasing Mo concentration. In the presence of segregated phosphorus and sulphur, this effect is expected to become even more pronounced.

Consequently, the inter-dendritic regions in HT2 retain liquid to lower temperatures than those in HT1, resulting in prolonged grain-boundary wetting and reduced resistance to crack formation. These observations demonstrate that local liquid stability provides a more meaningful indication of cracking susceptibility than the bulk solidification range.

4.4 Solidification cracking

The Transvarestraint results reveal a clear difference in solidification cracking susceptibility between HT1 and HT2, as reflected by their MCL and TCL values. Cracks were observed to initiate and propagate preferentially along inter-dendritic regions, confirming the critical role of residual liquid films in crack formation. Compared with Alloy D9, both D9I heats exhibited significantly greater cracking susceptibility. The increase in TCL and MCL exceeded threefold despite only modest increases in phosphorus, silicon and boron contents. This observation highlights the strong influence of minor alloying elements on weldability. These findings indicate that cracking susceptibility is governed primarily by the chemistry, continuity and persistence of inter-dendritic liquid films rather than by the bulk freezing range alone.

4.5 Mechanism of Solidification Cracking

Based on the combined thermodynamic modelling, microstructural characterisation and Varestraint testing results, a chemistry-controlled mechanism is proposed for solidification cracking in Alloy D9I.

An increase in the Ti/(C+0.856N) value modifies the solidification sequence through earlier precipitation of Ti(C,N), thereby altering the composition of the residual inter-dendritic liquid. This promotes enrichment of Mo, Si, P, Ti, S and other solute elements during the terminal stages of solidification. Although the overall solidification range changes only marginally, the local chemistry of the inter-dendritic liquid changes significantly, as shown in Fig. 13.

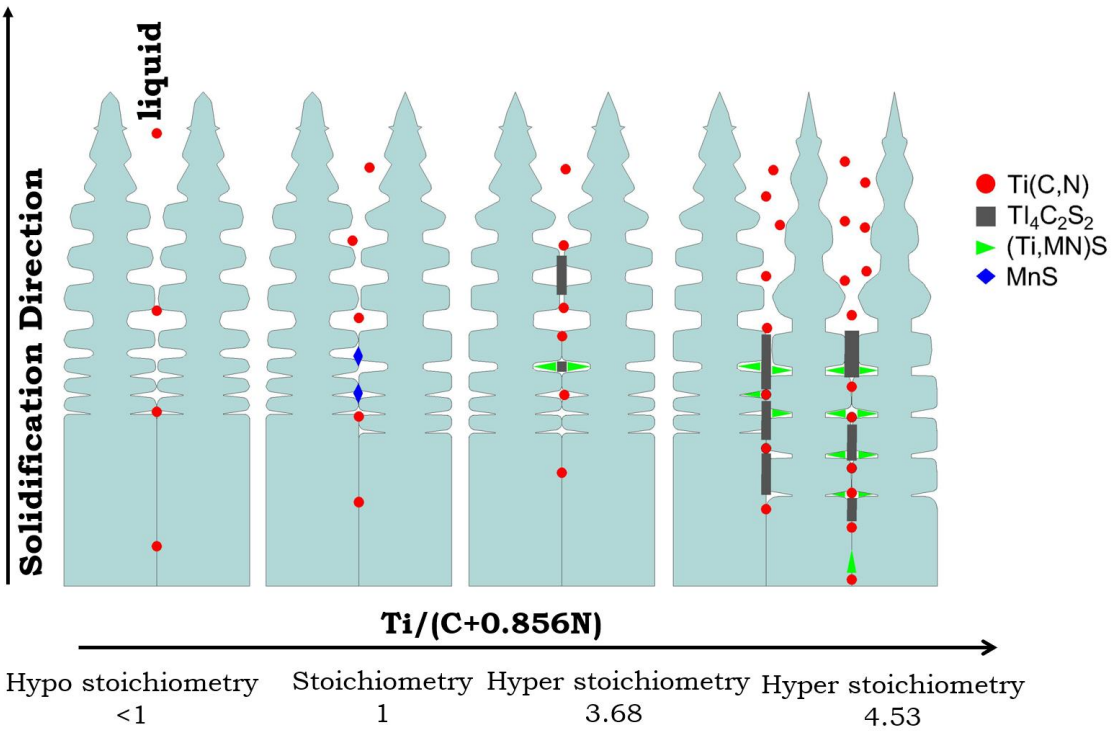


Fig.13. Schematic illustration of the nature of inter-dendritic eutectic phase formation during solidification in Alloy D9I with an increase in Ti/(C+0.856N), which leads to increased propensity to solidification cracking.

The resulting solute-enriched liquid films remain stable to lower temperatures and persist over a wider freezing range. During the final stages of solidification, these liquid films are unable to accommodate the imposed tensile strain, leading to crack initiation and propagation along dendrite boundaries. Therefore, careful optimisation of Ti/(C+0.856N) and strict control of minor alloying and impurity elements are essential for improving weldability and mitigating solidification cracking in D9I cladding alloys.

5. Conclusions

1. Alloy D9I exhibits significantly higher solidification cracking susceptibility than that reported for Alloy D9 and 316L(N) SS, as evidenced by the Varestraint test results.
2. Thermodynamic equilibrium and Scheil's solidification simulations indicate that the two D9I heats, with Ti/(C+0.856N) of 3.68 and 4.53, respectively, exhibit only marginal differences in their overall solidification ranges.
3. Despite the similar bulk solidification ranges, the D9I heat with a Ti/(C+0.856N) of 4.53 exhibits significantly higher solidification cracking susceptibility than the heat with a Ti/(C+0.856N) of 3.68.
4. The increased cracking susceptibility of the heat with a Ti/(C+0.856N) of 4.53 is attributed to modifications in the solidification path caused by earlier Ti(C,N) precipitation, which promotes enhanced segregation of alloying and impurity elements such as Mo, Ti, Si, P and S in the inter-dendritic liquid during the terminal stages of solidification.
5. Thermodynamic calculations and microstructural characterisation indicate that local inter-dendritic liquid chemistry, liquid stability, and grain-boundary cohesion play a more dominant role in governing solidification cracking susceptibility than the bulk solidification range alone.
6. The results demonstrate that careful control of Ti/(C+0.856N) ratio and minor alloying element concentrations is essential for mitigating solidification cracking and improving the weldability of Alloy D9

Acknowledgements

The authors are thankful to Prof. K.G. Pradeep, IIT Madras, Dr S. Amirthapandian, MSG and Ms Sreevidya, MMG, for extending their help in conducting SEM/EDS analysis.

Author Contribution: R. Ravikumar: Conceptualisation, Experiment, Data curation, validation, Preparation of manuscript; M. Divya: Numerical analysis, Data curation, review

of manuscript; S. Sampreeth: Numerical analysis and Data curation; C. R. Das: Supervision, Data Curation, Review of the manuscript.

Declarations:

Competing interests: The authors declare no competing interests.

Funding: The authors declare that no financial support was received for the research,

Declaration of Generative AI Use in the Writing Process

During the preparation of this manuscript, the authors used ChatGPT, developed by OpenAI, to assist with instructing and organising the paper's content. All outputs generated by the AI tool were carefully reviewed and edited by the authors. The authors take full responsibility for the conceptual framework, accuracy, integrity, and final content of the publication.

References

1. S. L. Mannan, S. C. Chetal, Baldev Raj and S. B. Bhoje, Selection of materials for prototype fast breeder reactor. (2000), Transactions- Indian Institute of Metals 56(2)
2. V. Shankar, T. P. S. Gill, S. L. Mannan and S. Sundaresan. (2003)Solidification cracking in austenitic stainless steel welds. Sadhana Vol. 28, Parts 3 & 4, pp. 359–382. https://link.springer.com/article/10.1007/BF02706438
3. Raj, B. (2009). Materials science research for sodium-cooled fast reactors. *Bull Mater Sci* 32, 271–283 https://doi.org/10.1007/s12034-009-0041-9
4. M. D. Mathew, K. A. Gopal, S. Murugan, B. K. Panigrahi, A. K. Bhaduri, and T. Jayakumar,(2013) Development of IFAC-1 SS: An Advanced Austenitic Stainless Steel for Cladding and Wrapper Tube Applications in Sodium-cooled Fast Reactors, Advanced Material Research, ISSN:1662-8985, Vol. 794, pp 749-7756,10.4028/www.scientific.net/AMR.794.749
5. Baldev Raj, Divakar Ramachandran, M. Vijayalakshmi, (2009) Development of Cladding Materials for Sodium Cooled Fast Reactors in India, Special Issue on High Performance Structural Materials, Trans. Ind. Inst. Met., 62(2) 89-94.
6. K. Liu, P. Yu, and S. Kou, (2020) Solidification Cracking Susceptibility of Stainless Steels: New Test and Explanation, Supplement to the Welding Journal, 2020.https://doi.org/10.29391/2020.99.024
7. Kota Kadoi,Akira Fujinaga, Motomichi Yamamoto and Kenji Shinozak, (2013) “The effect of welding conditions on solidification cracking susceptibility of type 310S stainless steel during laser welding an in-situ observation technique”, Weld in the World 57:383-390.
8. J. Yu, M. Romouts, G. Maes,(2013) Cracking behavior and mechanical properties of austenitic stainless steel parts produced by laser metal deposition. Materials and Design, http://dx.doi.org/10.1016/j.matdes.2012.08.078
9. Joonoh Moona,et al ,(2020). Owing to the extremely low solubility of boron in iron, its addition further increases susceptibility to solidification cracking. Material characterisation. doi.org/10.1016/j.matchar.2020.110319.

10. Baldev Raj, S. L. Mannan, P. R. Vasudeva Rao and M. D. Mathew "(2002) Development of fuels and structural materials for fast breeder reactors. Sadhana Vol. 27, Part 5, October 2002, pp. 527–558.
11. Shotaro Yamashita, Ryohei Yamauchi & Kazuyoshi Saida (2022). Influence mechanism of solidification mode on solidification cracking susceptibility of stainless steel, Welding International, 36:11, 693-704, DOI: 10.1080/09507116.2022.2124747.
12. Srinivasan. G., Bhaduri. A.K., Shankar. V. et al. (2008) Evaluation of Hot Cracking Susceptibility of Some Austenitic Stainless Steels and a Nickel-Base Alloy. Weld World 52, 4–17 (2008). https://doi.org/10.1007/BF03266647.
13. KUJANPÄÄ, V., SUUTALA, N., TAKALO, T., MOISIO, T. (1979) Correlation between solidification cracking and microstructure in austenitic-ferritic stainless steel, Welding Research International 9 (1979) 55–76.
14. Suresh Varma, P. V., Gupta, A., Amit, K., Bhatt, R. B., Afzal, M., Panakkal, J. P., Kamath, H. S., & Bhabha Atomic Research Centre, Mumbai (India). (2009). Pulsed Nd-YAG laser welding of Prototype Fast Breeder Reactor fuel elements
15. Bhaduri, A.K., Srinivasan, G., Klenk, A. et al. (2009). Study of Hot Cracking Behaviour of 14Cr-15Ni-2.5Mo Ti-Modified Fully Austenitic Stainless Steels using Varestraint and Hot Ductility Tests. Weld World 53, 17–27 https://doi.org/10.1007/BF03266688
16. Haraprasanna Tripathy, S. Raju, Arun Kumar Rai, G. Panneerselvam, T. Jayakumar (2013) Thermal stability and thermal property characterisation of Fe–14.4Cr–15.4Ni–2.4Mo–2.36Mn 0.25Ti1.02Si–0.042C–0.04P–0.005B (mass%) austenitic stainless steel (Alloy D9I), Nuclear Engineering And Design, Volume 255,2013, Pages 86-96,
17. Urélie Jacob, Christophe Domain, Gilles Adjanor, Patrick Todeschini, Erwin Povoden-Karadeniz, (2020) Thermodynamic modelling of G-phase and assessment of phase stabilities in reactor pressure vessel steels and cast duplex stainless steels, Journal of Nuclear Materials Volume 533,2020,152091,ISSN 0022-3115, https://doi.org/10.1016/j.jnucmat.2020.152091
18. Melaragno, G.S., Alexandrov, B.T(2026). Hot cracking susceptibility evaluation for alloy design and wire arc additive manufacturing of functionally graded materials for harsh service environments. Weld World https://doi.org/10.1007/s40194-026-02353-x
19. Folkhard E (1988)Welding metallurgy of stainless steels (NewYork: Springer Verlag)
20. Matsuda F, NakagawaH, Lee J B (1989) A weld cracking in duplex stainless steel (Report II) – modelling of cellular dendritic growth during weld solidification. *Trans. Jpn. Weld. Res. Inst.* 18: 107–117
21. Froes, F. H **(**2015**).** Titanium Physical Metallurgy, Processing, and Applications, ASM International.
22. Welding Metallurgy by Sindo Kou. 2003 (Second edition)